Inorg. Chem. **2008**, *47*, 8429−8436

Forum

Recent Progress in Oxide Thermoelectric Materials: p-Type $Ca_3Co_4O_9$ and n-Type $SrTiO_3$

Hiromichi Ohta,* Kenji Sugiura, and Kunihito Koumoto

Graduate School of Engineering, Nagoya University, Furo-cho, Chikusa, Nagoya 464-8603, Japan, and CREST, Japan Science and Technology Agency, 4-1-8 Honcho, Kawaguchi 332-0012, Japan

Received April 10, 2008

Thermoelectric energy conversion technology to convert waste heat into electricity has received much attention. In addition, metal oxides have recently been considered as thermoelectric power generation materials that can operate at high temperatures on the basis of their potential advantages over heavy metallic alloys in chemical and thermal robustness. We have fabricated high-quality epitaxial films composed of oxide thermoelectric materials that are suitable for clarifying the intrinsic "real" properties. This review focuses on the thermoelectric properties of two representative oxide epitaxial films, p-type $Ca_3Co_4O_9$ and n-type $SrTiO_3$, which exhibit the best thermoelectric figures of merit, ZT ($=S^2\sigma T\kappa^{-1}$, S = Seebeck coefficient, σ = electrical conductivity, κ = thermal conductivity, and T = absolute temperature) among oxide thermoelectric materials reported to date. In addition, we introduce the recently discovered giant S of two-dimensional electrons confined within a unit cell layer thickness (∼0.4 nm) of $SrTiO_3$.

1. Introduction

Today, most energy resources are discharged as waste heat into the environment without practical applications. Such exhaust heat is approximately 60% energy. Hence, thermoelectric energy conversion technology to convert waste heat into electricity has received much attention. In 1821, Seebeck initially discovered the principle of thermoelectric energy conversion[1] when he found that introducing a temperature difference across a bar generated a voltage between the two ends of a metal bar. Thus, when electric loads are connected at both ends of a metal bar, electric current can be obtained.

In order to realize an efficient thermoelectric energy conversion, the following three physical properties are required for thermoelectric materials: (1) low thermal conductivity (κ), which is necessary to introduce a large temperature difference into both ends of the material, (2) high electrical conductivity (σ), which is required to reduce the internal resistance of the material, and (3) large thermoelectromotive force (Seebeck coefficient, S), which is needed to obtain a high voltage.

Generally, the performance of a thermoelectric material is evaluated in terms of the dimensionless figure of merit, $ZT = S^2\sigma T\kappa^{-1}$, where Z and T are the figure of merit and the absolute temperature, respectively. For practical thermoelectric applications, thermoelectric materials with $ZT > 1$ are required.[2]

Figure 1 summarizes the $ZT-T$ curves for conventional "heavy-metal-based" thermoelectric materials. The ZT values of several materials, including Bi_2Te_3 and PbTe, exceed 1 and are sufficient for practical applications.[2–8] However, these materials are not attractive, particularly when operating at high temperatures ($T \sim 1000$ K), because their constituents can easily decompose, vaporize, or melt at high temperatures.

* Corresponding author. E-mail: h-ohta@apchem.nagoya-u.ac.jp.

(1) Seebeck, T. J.; Abh, K. *Akad. Wiss.* **1823**, 265.
(2) Tritt, T. M.; Subramanian, M. A.; Bottner, H.; Caillat, T.; Chen, G.; Funahashi, R.; Ji, X.; Kanatzidis, M.; Koumoto, K.; Nolas, G. S.; Poon, J.; Rao, A. M.; Terasaki, I.; Venkatasubramanian, R.; Yang, J. *MRS Bull.* **2006**, *31*, 188, and references cited therein (special issue on harvesting energy through thermoelectrics: power generation and cooling)
(3) Mahan, G.; Sales, B.; Sharp, J. *Phys. Today* **1997**, *50*, 42.
(4) DiSalvo, F. J. *Science* **1999**, *285*, 703.
(5) Rupprech., J.; Maier, R. G. *Phys. Status Solidi* **1965**, *8*, 3.
(6) Wright, D. A. *Nature* **1958**, *181*, 834.
(7) Hsu, K. F.; Loo, S.; Guo, F.; Chen, W.; Dyck, J. S.; Uher, C.; Hogan, T.; Polychroniadis, E. K.; Kanatzidis, M. G. *Science* **2004**, *303*, 818.
(8) Abeles, B.; Cohen, R. W. *J. Appl. Phys.* **1964**, *35*, 247.

10.1021/ic800644x CCC: $40.75
Published on Web 09/29/2008

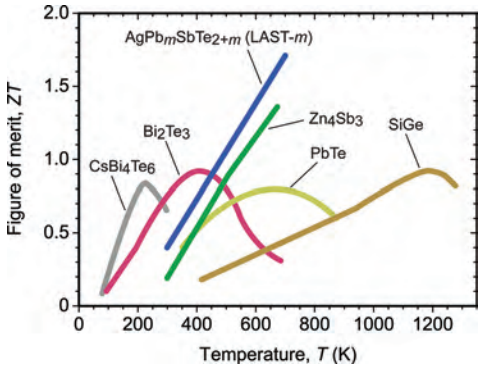

Figure 1. Thermoelectric figure of merit, Z, vs temperature for conventional heavy-metal-based materials.

Furthermore, employing these heavy metals should be limited to specific environments such as space because they are usually toxic, low in abundance as natural resources, and thus not environmentally benign.

On the basis of this background, metal oxides have recently attracted much attention as thermoelectric power generation materials at high temperatures on the basis of their potential advantages over heavy metallic alloys in chemical and thermal robustness.[9] Although there are numerous reports on the thermoelectric properties of metal oxides, the intrinsic properties are difficult to determine because most reported materials are very small single crystals and/or polycrystalline ceramics, which are composed of nonoriented grains with many grain boundaries, pores, and impurities. Therefore, to clarify the intrinsic thermoelectric properties of oxides, we have fabricated high-quality epitaxial films of several thermoelectric oxides, including Na_xCoO_2,[10–12] Li_xCoO_2,[13] Sr_xCoO_2,[14] Ca_xCoO_2,[15] $Ca_3Co_4O_9$,[15,16] $SrTiO_3$:Nb,[17] TiO_2:Nb,[18] and $SrO(SrTiO_3)$:Nb.[19] This review focuses on the thermoelectric properties of two representative oxides, p-type $Ca_3Co_4O_9$ and n-type $SrTiO_3$:Nb, which exhibit the best ZT among oxide thermoelectric materials reported to date. Additionally, we introduce the recently discovered giant thermoelectric Seebeck coefficient of two-dimensional (2D) electrons confined within a unit cell layer thickness (~0.4 nm) of $SrTiO_3$.[20–22]

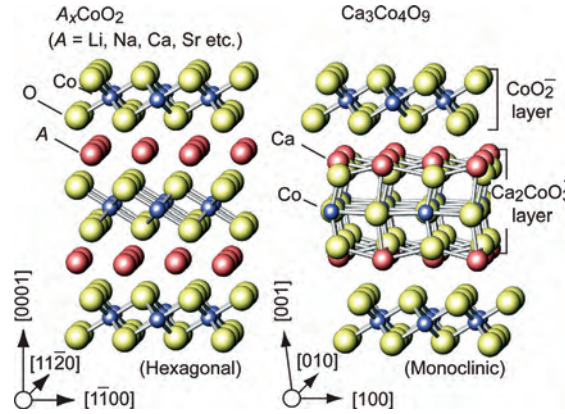

Figure 2. Schematic crystal structures of layered cobalt oxides. Left: A_xCoO_2 (A = Li, Na, Ca, Sr). Right: $Ca_3Co_4O_9$. Both crystals have CoO_2^- layers composed of edge-shared CoO_6 octahedra.

2. p-Type Layered Cobalt Oxide: $Ca_3Co_4O_9$

Figure 2 schematically depicts the crystal structures of (left) A_xCoO_2 (A = Li, Na, Ca, Sr; the x value of Na_xCoO_2 was varied from 0.3 to 0.9)[23,24] and (right) $Ca_3Co_4O_9$. The A_xCoO_2 crystal was composed of alternating stacks of a CdI_2-type CoO_2^- layer and an A^+ or A^{2+} layer along the c axis, whereas the $Ca_3Co_4O_9$ crystal was composed of a CoO_2^- layer and a rock-salt-type $Ca_2CoO_3^+$ layer.[25] Because hole carrier conduction occurs predominantly in the CoO_2^- layer,[26] c-axis-oriented epitaxial films are preferable for determining the intrinsic thermoelectric properties.

Generally, a vapor-phase epitaxy (VPE) method, such as pulsed-laser deposition (PLD), is appropriate for high-quality epitaxial film growth of oxide materials. However, fabrication of a Na_xCoO_2 epitaxial film is very difficult by a conventional VPE method (growth temperature, $T_g \sim 700$ °C) because revaporization of Na due to its extremely a large vapor pressure of $\sim 10^4$ Pa at 700 °C occurs during film growth. In our preliminary experiment, films composed of (111)-oriented Co_3O_4 (cubic spinel-type) and (0001)-oriented Na_xCoO_2 were grown on a (0001)-oriented α-Al_2O_3 substrate at lower T_g (100 °C < T_g < 500 °C) by the PLD method using a $Na_{0.7}CoO_2$ ceramic target, while epitaxial films of (111)-oriented CoO (cubic NaCl-type) were grown at higher T_g (600 °C < T_g < 800 °C).

Thus, to fabricate c-axis-oriented epitaxial films of layered cobalt oxides, we used a specialized film growth method of *reactive solid-phase epitaxy* (R-SPE),[10] which is a powerful means to fabricate single-crystalline films of layered oxides,[27,28] and subsequent topotactic ion exchange. First, a high-quality epitaxial film of CoO was deposited on the (0001) face of an α-Al_2O_3 substrate at 700 °C by PLD using a Co_3O_4 sintered disk as a target. Then the PLD-deposited

(9) Koumoto, K.; Terasaki, I.; Funahashi, R. *MRS Bull.* **2006**, *31*, 206.
(10) Ohta, H.; Kim, S. W.; Ohta, S.; Koumoto, K.; Hirano, M.; Hosono, H. *Cryst. Growth Des.* **2005**, *5*, 25.
(11) Ohta, H.; Mizutani, A.; Sugiura, K.; Hirano, M.; Hosono, H.; Koumoto, K. *Adv. Mater.* **2006**, *18*, 1649.
(12) Ishida, Y.; Ohta, H.; Fujimori, A.; Hosono, H. *J. Phys. Soc. Jpn.* **2007**, *76*, 103709.
(13) Mizutani, A.; Sugiura, K.; Ohta, H.; Koumoto, K. *Cryst. Growth Des.* **2008**, *8*, 755.
(14) Sugiura, K.; Ohta, H.; Nomura, K.; Hirano, M.; Hosono, H.; Koumoto, K. *Appl. Phys. Lett.* **2006**, *88*, 082109.
(15) Sugiura, K.; Ohta, H.; Nomura, K.; Hirano, M.; Hosono, H.; Koumoto, K. *Appl. Phys. Lett.* **2006**, *89*, 032111.
(16) Sugiura, K.; Ohta, H.; Nomura, K.; Saito, T.; Ikuhara, Y.; Hirano, M.; Hosono, H.; Koumoto, K. *Mater. Trans.* **2007**, *48*, 2104.
(17) Ohta, S.; Nomura, T.; Ohta, H.; Hirano, M.; Hosono, H.; Koumoto, K. *Appl. Phys. Lett.* **2005**, *87*, 092108.
(18) Kurita, D.; Ohta, S.; Sugiura, K.; Ohta, H.; Koumoto, K. *J. Appl. Phys.* **2006**, *100*, 096105.
(19) Lee, K. H.; Ishizaki, A.; Kim, S. W.; Ohta, H.; Koumoto, K. *J. Appl. Phys.* **2007**, *102*, 033702.
(20) Ohta, H.; Kim, S. W.; Mune, Y.; Mizoguchi, T.; Nomura, K.; Ohta, S.; Nomura, T.; Nakanishi, Y.; Ikuhara, Y.; Hirano, M.; Hosono, H.; Koumoto, K. *Nat. Mater.* **2007**, *6*, 129.
(21) Mune, Y.; Ohta, H.; Koumoto, K.; Mizoguchi, T.; Ikuhara, Y. *Appl. Phys. Lett.* **2007**, *91*, 192105.
(22) Lee, K. H.; Mune, Y.; Ohta, H.; Koumoto, K. *Appl. Phys. Express* **2008**, *1*, 015007.
(23) Fouassier, C.; Matejka, G.; Reau, J. M.; Hagenmuller, P. *J. Solid State Chem.* **1973**, *6*, 532.
(24) Huang, Q.; Foo, M. L.; Pascal, R. A.; Lynn, J. W.; Toby, B. H.; He, T.; Zandbergen, H. W.; Cava, R. J. *Phys. Rev. B* **2004**, *70*, 184110.
(25) Miyazaki, Y.; Onoda, M.; Oku, T.; Kikuchi, M.; Ishii, Y.; Ono, Y.; Morii, Y.; Kajitani, T. *J. Phys. Soc. Jpn.* **2002**, *71*, 491.
(26) Terasaki, I.; Sasago, Y.; Uchinokura, K. *Phys. Rev. B* **1997**, *56*, 12685.

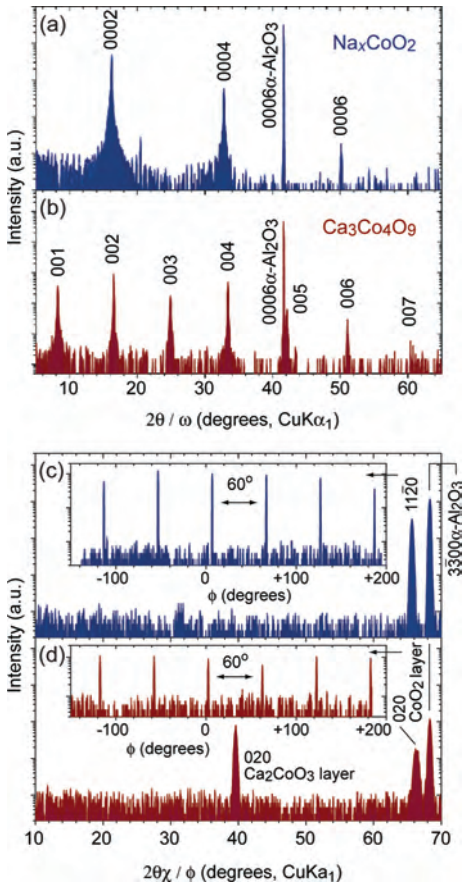

Figure 3. XRD patterns of (a and c) Na_xCoO_2 and (b and d) $Ca_3Co_4O_9$ epitaxial films.

CoO film was heated together with a $NaHCO_3$ powder at 700 °C in air to give a *c*-axis-oriented Na_xCoO_2 ($x \sim 0.8$) epitaxial film. The Na_xCoO_2 film can be converted into Li_xCoO_2,[13] Sr_xCoO_2,[14] Ca_xCoO_2,[15] and $Ca_3Co_4O_9$[15,16] epitaxial films by the appropriate ion-exchange treatment. Details of our film growth method are described elsewhere.[10,11,13–16,27,28]

Crystalline quality and orientation of the film were analyzed by high-resolution X-ray diffraction (HR-XRD, ATX-G, Cu Kα_1, Rigaku Co.). The out-of-plane XRD pattern (synchronous scan of 2θ and ω in the horizontal plane), in-plane XRD pattern (synchronous scan of $2\theta\chi$ and ϕ in the azimuthal plane), out-of-plane rocking curve (2θ fixed ω scan), and in-plane rocking curve (IXRC; $2\theta\chi$ fixed ϕ scan) were obtained. The surface morphology was observed using atomic force microscopy (AFM).

Figure 3 (upper panel) shows the out-of-plane Bragg XRD patterns of (a) Na_xCoO_2 and (b) $Ca_3Co_4O_9$ films. Intense Bragg diffraction peaks of $000l$ Na_xCoO_2 were observed along with 0006 α-Al_2O_3 in Figure 3a, indicating a highly *c*-axis-oriented film. The chemical composition of the film was evaluated as $Na_{0.83}CoO_2$ by X-ray fluorescence (ZSX 100e, Rigaku Co.) analysis. After the ion-exchange treatment of Na^+ with Ca^{2+},[29] the XRD pattern dramatically changed as shown in Figure 3b, indicating that the $Na_{0.83}CoO_2$ epitaxial film was converted into a highly *c*-axis-oriented $Ca_3Co_4O_9$ film upon the ion-exchange treatment.

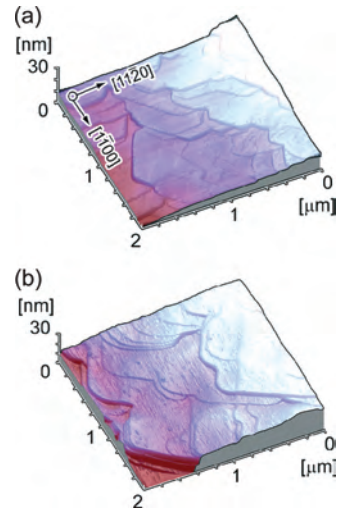

Figure 4. Topographic AFM images of (a) Na_xCoO_2 and (b) $Ca_3Co_4O_9$ epitaxial films.

Figure 3 (lower panel) shows the in-plane Bragg XRD patterns of (c) Na_xCoO_2 and (d) $Ca_3Co_4O_9$ films. Although only intense Bragg peaks of $11\bar{2}0$ $Na_{0.83}CoO_2$ and $3\bar{3}00$ α-Al_2O_3 were observed in Figure 3c, Figure 3d had two independent Bragg peaks at $2\theta\chi/\phi \sim 40$ and 66°. The independent Bragg peaks correspond to the 020 diffractions of the rock-salt-type Ca_2CoO_3 layer ($b_1 = 0.455$ nm) and that of the CdI_2-type CoO_2 layer ($b_2 = 0.282$ nm), respectively, because of the fact that $Ca_3Co_4O_9$ is composed of these two layers with different lattice constants along the *b* axis.[25] Parts c and d of Figure 3 clearly show 6-fold symmetrical IXRC, indicating that topotactic ion exchange from Na^+ to Ca^{2+} occurred.

Figure 4 shows the topographic AFM images of (a) $Na_{0.8}CoO_2$ and (b) $Ca_3Co_4O_9$ films. Both parts a and b of Figure 4 show a steplike structure composed of several flakelike domains, but only Figure 4a shows hexagonal-shaped domains, whereas Figure 4b has several square-shaped domains (~ 1 μm^2) due to the monoclinic crystal symmetry of $Ca_3Co_4O_9$. These features in the $Ca_3Co_4O_9$ film are similar to those in the $Na_{0.83}CoO_2$ film, indicating that the framework composed of epitaxial CoO_2 layers is maintained during this process and that the $Na_{0.83}CoO_2$ epitaxial film is successfully converted into a $Ca_3Co_4O_9$ epitaxial film by the topotactic ion-exchange method.

Figure 5 summarizes the thermoelectric properties of a p-type $Ca_3Co_4O_9$ epitaxial film [(a) $|S|-T$ curves, (b) $\sigma-T$ curves, (c) $S^2\sigma-T$ curves, (d) $\kappa-T$ curves, and (e) $ZT-T$ curves]. For comparison, several values of $Ca_3Co_4O_9$ from the literature [1, single crystal (Masset et al., 2000,[30] and Limelette et al., 2005[31]); 2, single crystal (Shikano and

(27) Ohta, H.; Nomura, K.; Orita, M.; Hirano, M.; Ueda, K.; Suzuki, T.; Ikuhara, Y.; Hosono, H. *Adv. Funct. Mater.* **2003**, *13*, 139.
(28) Nomura, K.; Ohta, H.; Ueda, K.; Kamiya, T.; Hirano, M.; Hosono, H. *Science* **2003**, *300*, 1269.
(29) Cushing, B. L.; Wiley, J. B. *J. Solid State Chem.* **1998**, *141*, 385.
(30) Masset, A. C.; Michel, C.; Maignan, A.; Hervieu, M.; Toulemonde, O.; Studer, F.; Raveau, B.; Hejtmanek, J. *Phys. Rev. B* **2000**, *62*, 166.
(31) Limelette, P.; Hardy, V.; Auban-Senzier, P.; Jerome, D.; Flahaut, D.; Hebert, S.; Fresard, R.; Simon, C.; Noudem, J.; Maignan, A. *Phys. Rev. B* **2005**, *71*, 233108.

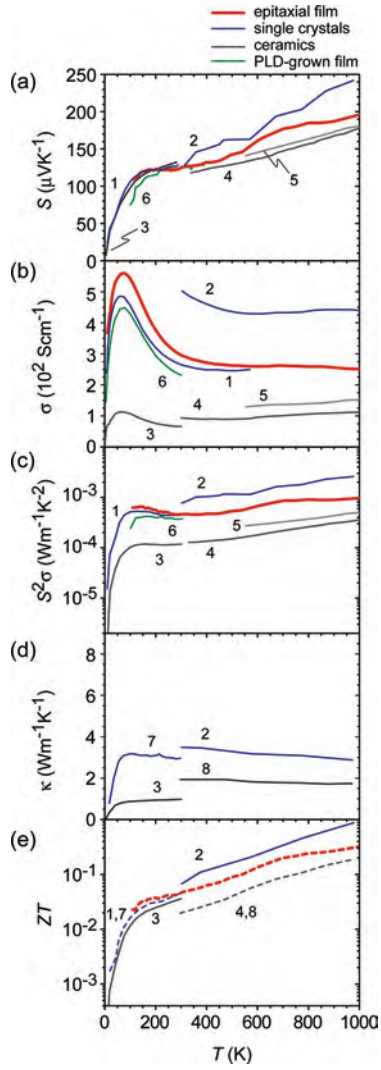

Figure 5. Thermoelectric properties of [(a) $|S|-T$ curves, (b) $\sigma-T$ curves, (c) $S^2\sigma-T$ curves, (d) $\kappa-T$ curves, and (e)$ZT-T$ curves] of p-type $Ca_3Co_4O_9$ [1, single crystal (Masset et al., 2000,[30] and Limelette et al., 2005[40]); 2, single crystal (Shikano and Funahashi, 2003[32]); 3, ceramic (Miyazaki et al., 2000[33]); 4, ceramic (Xu et al., 2002[34]); 5, ceramic (Itahara, 2004[35]); 6, film (Hu et al., 2005[36]); 7, single crystal (Satake et al., 2004[37]); 8, ceramic (Li et al., 2000[38])].

Funahashi, 2003[32]); 3, ceramic (Miyazaki et al., 2000[33]); 4, ceramic (Xu et al., 2002[34]); 5, ceramic (Itahara, 2004[35]); 6, film (Hu et al., 2005[36]); 7, single crystal (Satake et al., 2004[37]); 8, ceramic (Li et al., 2000[38])] are also plotted in the figure.

The S values were positive, indicating p-type conductivity (Figure 5a). The S values of the epitaxial film were similar to those of bulk samples and other films, suggesting that all of these samples have the same hole concentration. The epitaxial film and polycrystalline ceramic had a negligible difference, which is probably due to the orientation of the crystal because $Ca_3Co_4O_9$ has some anisotropy in S.[39] On the other hand, large differences were observed between the σ values of the samples (Figure 5b). The σ values of the epitaxial film were several times higher than those of ceramics but were comparable to those of single crystals, suggesting that carrier scattering by the grain boundaries is almost completely eliminated in the film. Furthermore, the σ values of the fabricated film were higher than any other reported values in films grown by conventional methods,[36,39–41] indicating that the fabricated film by R-SPE is a high-quality epitaxial film. The high conductivity of the epitaxial film leads to a high power factor ($S^2\sigma$) of $\sim 10^{-3}$ $W\cdot m^{-1}\cdot K^{-2}$ over a temperature range of 100−1000 K as shown in Figure 5c.

The results of the bulk materials ($\kappa \sim 3$ $W\cdot m^{-1}\cdot K^{-1}$ in single crystal and $\kappa < 2$ $W\cdot m^{-1}\cdot K^{-1}$ in the polycrystal) suggest that the κ values of $Ca_3Co_4O_9$ are nearly independent of temperature (Figure 5d). Thus, we calculated the ZT values of the epitaxial film assuming that the κ value was 3 $W\cdot m^{-1}\cdot K^{-1}$ in the temperature range of 100−1000 K. The ZT value of the epitaxial film increased gradually with temperature and reached ~0.3 at 1000 K (Figure 5e). This value is lower than that of conventional alloyed metals such as p-type Si−Ge ($ZT \sim 0.8$),[42] although it is higher than any other ZT values for p-type oxides. However, further improving the thermoelectric performance in p-type $Ca_3Co_4O_9$ is essential through, for instance, nanostructural design such as the control of the misfit ratio because it has been reported that the misfit ratio of these misfit-layered cobalt oxides can lead to an improvement of the S value while keeping the carrier concentration.[43]

3. n-Type Electron-Doped $SrTiO_3$:Nb

Among the several n-type oxides proposed to date such as Al-doped ZnO,[44] $In_2O_3(ZnO)_m$ (m = integer),[45] $CaMnO_3$,[46] and $SrTiO_3$,[47–49] we focused on heavily electron-doped $SrTiO_3$ as a promising candidate for an n-type material because it exhibits a rather large $|S|$ due to the large density

(32) Shikano, M.; Funahashi, R. *Appl. Phys. Lett.* **2003**, *82*, 1851.
(33) Miyazaki, Y.; Kudo, K.; Akoshima, M.; Ono, Y.; Koike, Y.; Kajitani, T. *Jpn. J. Appl. Phys.* **2000**, *39*, L531.
(34) Xu, G. J.; Funahashi, R.; Shikano, M.; Matsubara, I.; Zhou, Y. Q. *Appl. Phys. Lett.* **2002**, *80*, 3760.
(35) Itahara, H. Ph.D. Thesis, Nagoya University, Nagoya, Japan, 2004.
(36) Hu, Y. F.; Si, W. D.; Sutter, E.; Li, Q. *Appl. Phys. Lett.* **2005**, *86*, 082103.
(37) Satake, A.; Tanaka, H.; Ohkawa, T.; Fujii, T.; Terasaki, I. *J. Appl. Phys.* **2004**, *96*, 931.
(38) Li, S. W.; Funahashi, R.; Matsubara, I.; Ueno, K.; Sodeoka, S.; Yamada, H. *Chem. Mater.* **2000**, *12*, 2424.
(39) Sakai, A.; Kanno, T.; Yotsuhashi, S.; Odagawa, A.; Adachi, H. *Jpn. J. Appl. Phys.* **2005**, *44*, L966.
(40) Minami, H.; Itaka, K.; Kawaji, H.; Wang, Q. J.; Koinuma, H.; Lippmaa, M. *Appl. Surf. Sci.* **2002**, *197*, 442.
(41) Yoshida, Y.; Kawai, T.; Takai, Y.; Yamaguchi, M. *J. Ceram. Soc. Jpn.* **2002**, *110*, 1080.
(42) Dismukes, J. P.; Ekstrom, L.; Steigmeier, E. F.; Kudman, I.; Beers, D. S. *J. Appl. Phys.* **1964**, *35*, 2899.
(43) Ishiwata, S.; Terasaki, I.; Kusano, Y.; Takano, M. *J. Phys. Soc. Jpn.* **2006**, *75*, 104716.
(44) Ohtaki, M.; Tsubota, T.; Eguchi, K.; Arai, H. *J. Appl. Phys.* **1996**, *79*, 1816.
(45) Ohta, H.; Seo, W.-S.; Koumoto, K. *J. Am. Ceram. Soc.* **1996**, *79*, 2193.
(46) Matsubara, I.; Funahashi, R.; Takeuchi, T.; Sodeoka, S.; Shimizu, T.; Ueno, K. *Appl. Phys. Lett.* **2001**, *78*, 3627.
(47) Frederikse, H. P. R.; Thurber, W. R.; Hosler, W. R. *Phys. Rev.* **1964**, *134*, A442.
(48) Okuda, T.; Nakanishi, K.; Miyasaka, S.; Tokura, Y. *Phys. Rev. B* **2001**, *63*, 113104.
(49) Ohta, S.; Nomura, T.; Ohta, H.; Koumoto, K. *J. Appl. Phys.* **2005**, *97*, 034106.
(50) Ishida, Y.; Eguchi, R.; Matsunami, M.; Horiba, K.; Taguchi, M.; Chainani, A.; Senba, Y.; Ohashi, H.; Ohta, H.; Shin, S. *Phys. Rev. Lett.* **2008**, *100*, 056401.

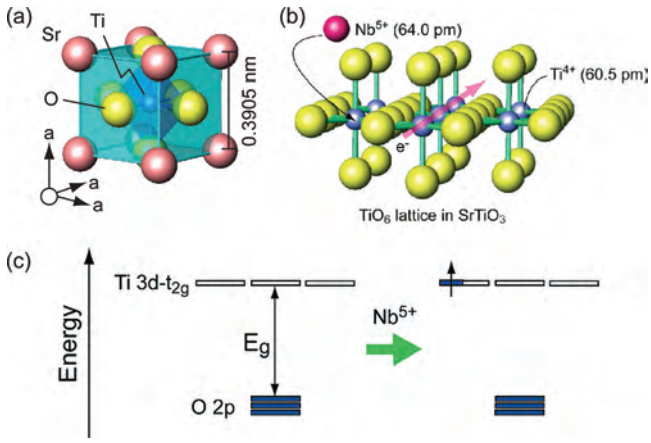

Figure 6. (a and b) Schematic crystal structure and (c) doping mechanism of $SrTiO_3$.

of states (DOSs) effective mass (m_d^* = carrier effective mass; m^* × band degeneracy × spin degeneracy = $6-10m_0$).[47] Moreover, bulk single crystals of heavily La-doped $SrTiO_3$ ($n_e \sim 10^{21}$ cm^{-3}) have recently been found to possess a large power factor (PF = $S^2\sigma$) of 3.6 × 10^{-3} W•m^{-1}•K^{-2} at room temperature,[48] which is comparable to that of a practical Peltier material, Bi_2Te_3, with a low carrier concentration ($n_e \sim 10^{19}$ cm^{-3}).[2] Furthermore, because the melting point of $SrTiO_3$ is very high (2080 °C), electron-doped $SrTiO_3$ crystals may be applicable at high temperatures (~1000 K).

$SrTiO_3$ is a popular metal oxide with a cubic perovskite structure (lattice parameter, a = 0.3905 nm), as shown in Figure 6a. All of the constituents of $SrTiO_3$ are rich in natural resources. Furthermore, the electrical conductivity of $SrTiO_3$ can be easily controlled from insulator to metal by substitutional doping of La^{3+} or Nb^{5+} (Figure 6b,c; for a detailed photoemission study of electron-doped $SrTiO_3$, see ref 50). We have examined the carrier transport properties of Nb- and La-doped $SrTiO_3$ single crystals ($n_e \sim 10^{20}$ cm^{-3}) at high temperatures (~1000 K) to clarify their intrinsic thermoelectric properties.[49] Although the experimental data suggest a relatively high ZT in heavily Nb-doped $SrTiO_3$, the maximum ZT could not be clarified because the solubility of the Nb^{5+} ions in the $SrTiO_3$ lattice is substantially smaller than the optimal concentration. In order to overcome this problem, we fabricated $SrTiO_3$ epitaxial films with ~10^{22} cm^{-3} Nb as a dopant and clarified that a 20% ($n_e \sim 3 \times 10^{21}$ cm^{-3}) Nb-doped $SrTiO_3$ epitaxial film exhibits $ZT \sim$ 0.37 at 1000 K, which is the largest value among n-type oxide semiconductors reported to date.[17]

Epitaxial films of Nb-doped $SrTiO_3$ were grown on the (001) face of $LaAlO_3$ single-crystalline substrates at 700 °C by PLD using $SrTiO_3$ targets containing up to 40% Nb as the dopant. Only intense Bragg XRD peaks of 002 $SrTiO_3$ and 002 $LaAlO_3$ were observed (Figure 7). Pendellosung fringes were clearly observed around the 002 $SrTiO_3$ peak, indicating high-crystalline qualities of the films. The lattice parameter of Nb-doped $SrTiO_3$ increased proportionally with the Nb concentration, implying that Nb^{5+} (64.0 pm) substitutes at the Ti^{4+} (60.5 pm) site. This site selectivity of Nb is also supported by the fact that Nb^{5+} ions act as donors.

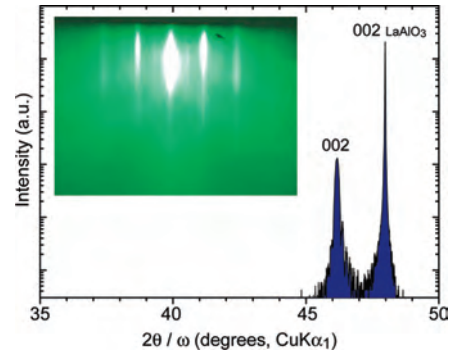

Figure 7. Out-of-plane XRD pattern of a 20% Nb-doped $SrTiO_3$ epitaxial film on the (001) face of the $LaAlO_3$ substrate. The inset shows the RHEED pattern (azimuth ⟨100⟩).

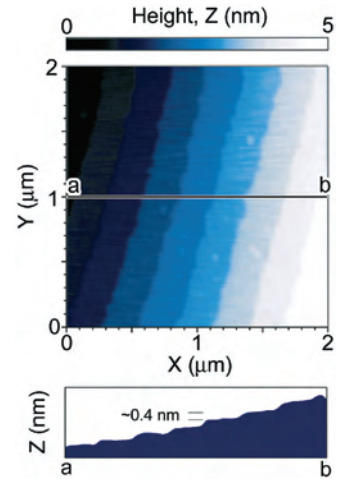

Figure 8. Topographic AFM image of a 20% Nb-doped $SrTiO_3$ epitaxial film.

Intense streak patterns were observed in the reflection high-energy electron diffraction (RHEED) pattern of the films (Figure 7, inset), indicating that the $SrTiO_3$:Nb films are heteroepitaxially grown on the (001) face of $LaAlO_3$. Atomically flat terraces and steps, which correspond to the unit cell height (~0.4 nm) of $SrTiO_3$:Nb, were clearly seen in the topographic AFM image of a $SrTiO_3$:Nb film (Figure 8). From these results, we conclude that the film quality is sufficient to evaluate thermoelectric properties.

Figure 9summarizes the thermoelectric properties of an n-type $SrTi_{0.8}Nb_{0.2}O_3$ epitaxial film [(a) $|S|-T$ curves, (b) $\sigma-T$ curves, (c) $S^2\sigma-T$ curves, (d) $\kappa-T$ curves, and (e) $ZT-T$ curves]. For comparison, the properties of several electron-doped $SrTiO_3$ [1, $Sr_{0.9}La_{0.1}TiO_3$ single crystal (Okuda et al., 2001[48]); 2, $Sr_{0.9}Y_{0.1}TiO_3$ (Obara et al., 2004[51]); 3, $Ba_{0.3}Sr_{0.6}La_{0.1}TiO_3$ ceramic (Muta et al., 2004[52]); 4, $Sr_{0.95}La_{0.05}TiO_3$ single crystal (Muta et al., 2005[53]); 5, $Ce_{0.2}Sr_{0.8}TiO_3$ epitaxial film (Ohtomo et al., 2007[54]); 6, $SrTi_{0.8}Nb_{0.2}O_3$ ceramic (Kato et al., 2007[55])] are also plotted. The $|S|$ value of the $SrTi_{0.8}Nb_{0.2}O_3$ epitaxial

(51) Obara, H.; Yamamoto, A.; Lee, C. H.; Kobayashi, K.; Matsumoto, A.; Funahashi, R. *Jpn. J. Appl. Phys.* **2004**, *43*, L540.
(52) Muta, H.; Kurosaki, K.; Yamanaka, S. *J. Alloys Compd.* **2004**, *368*, 22.
(53) Muta, H.; Kurosaki, K.; Yamanaka, S. *J. Alloys Compd.* **2005**, *392*, 306.
(54) Yamada, Y. F.; Ohtomo, A.; Kawasaki, M. *Appl. Surf. Sci.* **2007**, *254*, 768.

film gradually increased as the temperature increased (Figure 9a). The $|S|$ value of $SrTiO_3$ can be well expressed by the following equations:

$$S = -\frac{k_B}{e}\left(\frac{(r+2)F_{r+1}(\xi)}{(r+1)F_r(\xi)} - \xi\right) \quad (1)$$

where k_B, ξ, r [roughly $r = 0.5$ ($T < 750$) or $r = 0$ ($T > 750$ K)], and F_r are the Boltzmann constant, chemical potential, scattering parameter of the relaxation time, and Fermi integral, respectively. F_r is given by

$$F_r(\xi) = \int_0^\infty \frac{x^r}{1 + e^{x-\xi}}\,dx \quad (2)$$

The carrier concentration, n, is given by

$$n = 4\pi\left(\frac{2m_d{}^* k_B T}{h^2}\right)^{3/2} F_{1/2}(\xi) \quad (3)$$

where h, T, and $m_d{}^*$ (=[orbital degeneracy] × [spin degeneracy] × [effective mass] ≈ $7m_0$) are the Planck constant, absolute temperature, and DOS effective mass, respectively.

On the contrary, the σ value decreased with temperature (Figure 9b). The carrier electron concentration (n_e) of the $SrTi_{0.8}Nb_{0.2}O_3$ epitaxial film was ~2×10^{21} cm^{-3} and almost independent of temperature. Thus, the carrier mobility (μ) decreased proportionally to $T^{-2.0}$ below ~750 K and $T^{-1.5}$ above ~750 K, which is most likely because the dominant mechanism of carrier scattering changed as the temperature increased. The power factor ($S^2\sigma$) of the $SrTi_{0.8}Nb_{0.2}O_3$ epitaxial film above 200 K was nearly independent of the temperature (~1.5; Figure 9c).

Because κ measurements of a $SrTi_{0.8}Nb_{0.2}O_3$ epitaxial film are quite difficult, we measured the κ values of a $SrTi_{0.8}Nb_{0.2}O_3$ dense ceramic with a relative density of 92%, which was prepared by conventional solid-state sintering at 1500 °C in an argon atmosphere. Although a Schottky-type barrier at the grain boundary of dense ceramics significantly scatters the conduction electrons, the barrier does not affect the thermal conduction because most of the heat transport of $SrTi_{0.8}Nb_{0.2}O_3$ is dominated by the phonons (according to the Wiedemann−Franz law, the electron contribution is less than 15% of the total κ[17]). Therefore, dense $SrTi_{0.8}Nb_{0.2}O_3$ ceramics are applicable to the measurement of κ. The κ values of the $SrTi_{0.8}Nb_{0.2}O_3$ ceramic below 300 K were measured by a conventional steady-state method using a *Physical Property Measurement System* (Quantum Design), whereas above 300 K, they were measured by a laser flash method (thermal diffusivity) along with calorimetry (heat capacity).

Figure 9d shows the $\kappa-T$ curves for a $SrTi_{0.8}Nb_{0.2}O_3$ dense ceramic. In addition, the κ values for an undoped $SrTiO_3$ single crystal[53,56] are also plotted for comparison. The κ value of the $SrTi_{0.8}Nb_{0.2}O_3$ ceramic at room temperature was 8.8

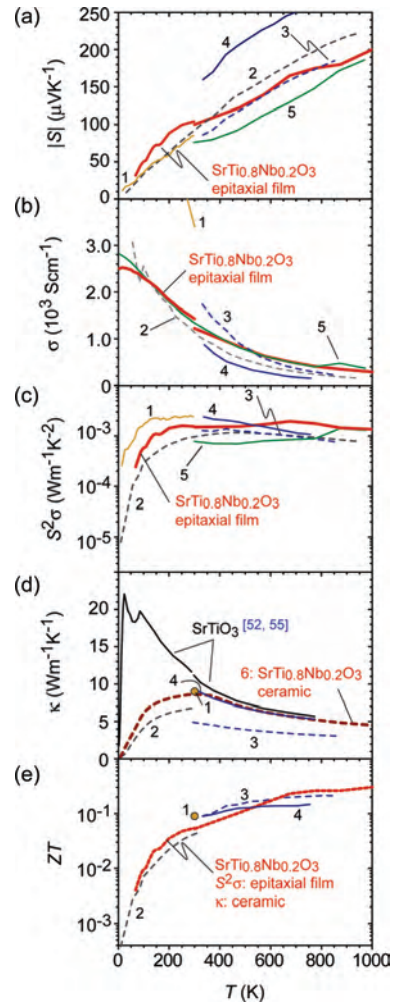

Figure 9. Thermoelectric properties [(a) $|S|-T$ curves, (b) $\sigma-T$ curves, (c) $S^2\sigma-T$ curves, (d) $\kappa-T$ curves, and (e) $ZT-T$ curves] of n-type electron-doped $SrTiO_3$ [1, $Sr_{0.9}La_{0.1}TiO_3$ single crystal (Okuda et al., 2001[47]); 2, $Sr_{0.9}Y_{0.1}TiO_3$ (Obara et al., 2004[51]); 3, $Ba_{0.3}Sr_{0.6}La_{0.1}TiO_3$ ceramic (Muta et al., 2004[52]); 4, $Sr_{0.95}La_{0.05}TiO_3$ single crystal (Muta et al., 2005[53]); 5, $Ce_{0.2}Sr_{0.8}TiO_3$ epitaxial film (Ohtomo et al., 2007[54]); 6, $SrTi_{0.8}Nb_{0.2}O_3$ ceramic (Kato et al., 2007[55])]. The κ values of undoped $SrTiO_3$[52,55] are also plotted for comparison.

$W \cdot m^{-1} \cdot K^{-1}$, which is 20% lower than that of the undoped $SrTiO_3$ single crystal, indicating that the dopant Nb^{5+} ion effectively reduces κ. The κ value gradually decreased with temperature because the phonon ZT values of the $SrTi_{0.8}Nb_{0.2}O_3$, which were calculated using $S^2\sigma$ values of the epitaxial film (Figure 9c) and κ values of the ceramic (Figure 9d), increased gradually with the temperature (Figure 9e). At 1000 K, the ZT value of $SrTi_{0.8}Nb_{0.2}O_3$ was ~0.3, which is smaller than that of heavy-metal-based materials. Thus, ZT must be significantly improved for practical thermoelectric applications of $SrTiO_3$. To improve the ZT value of $SrTiO_3$, the κ value must be reduced without decreasing $S^2\sigma$. Muta et al.[52,57] have reported that Sr^{2+}-site substitution of $SrTiO_3$ with Ca^{2+} or Ba^{2+} may be a good way to reduce the κ value of $SrTiO_3$. Their observation is

(55) Kato, K.; Yamamoto, M.; Ohta, S.; Muta, H.; Kurosaki, K.; Yamanaka, S.; Iwasaki, H.; Ohta, H.; Koumoto, K. *J. Appl. Phys.* **2007**, *102*, 116107.
(56) Suemune, Y. *J. Phys. Soc. Jpn.* **1965**, *20*, 174.
(57) Muta, H.; Ieda, A.; Kurosaki, K.; Yamanaka, S. *Mater. Lett.* **2004**, *58*, 3868.
(58) Yamamoto, M.; Ohta, H.; Koumoto, K. *Appl. Phys. Lett.* **2007**, *90*, 072101.

most likely because the introduction defects such as site substitutions and/or layered structures effectively reduces the κ value. However, Yamamoto et al.[57] have clarified that $S^2\sigma$ drastically decreases when Ca^{2+} and/or Ba^{2+} are substituted for Sr^{2+} in $SrTi_{0.8}Nb_{0.2}O_3$, indicating that Sr^{2+}-site substitution negatively affects the thermoelectric performance of $SrTi_{0.8}Nb_{0.2}O_3$. Thus, further improvements of the *ZT* value of $SrTi_{0.8}Nb_{0.2}O_3$ are nearly impossible in the conventional three-dimensional (3D) bulk state.

4. Giant Seebeck Coefficient of a 2D Electron Gas in $SrTiO_3$[20]

2D-confined electrons in extremely narrow (narrower than the de Broglie wavelength, $\lambda_D = h/\sqrt{3m^*k_BT}$, where h, m^*, and k_B are Planck's constant, the effective mass of a conductive electron or hole, and the Boltzmann constant, respectively) quantum wells exhibit exotic electron transport properties compared to the bulk materials due to the fact that the DOSs near the bottom of the conduction band and/or top of the valence band increase as the thickness of the quantum well decreases.[59] This phenomenon is called the "quantum size effect" and is applicable to a wide range of optoelectronic devices such as light-emitting and laser diodes.

In 1993, Hicks and Dresselhaus theoretically predicted that using superlattices can dramatically enhance the 2D thermoelectric figure of merit, $Z_{2D}T$, of a quantum well for thermoelectric semiconductors because only the S value increases with the DOSs of the quantum well, while σ and κ remain constant.[60] This model is based on the assumption that the enhancement of S^2 arises mainly from an increase in the DOSs near the conduction band edge where carrier electrons are confined to narrow spaces. Their prediction has been partly confirmed experimentally by employing a PbTe (1.5 nm)/$Pb_{0.927}Eu_{0.073}Te$ (45 nm) multiple quantum well,[60] which exhibited an $|S|$ value ~2.5 times larger than that of the corresponding 3D bulk. Hence, it is hypothesized that conduction carrier electrons are localized more strongly in $SrTiO_3$ than in heavy-metal semiconductors because $SrTiO_3$ is basically an insulator. In other words, 2D electron confinement may effectively and significantly enhance the $|S|$ value of $SrTiO_3$.

We fabricated several superlattices composed of insulating $SrTiO_3$ (undoped, conduction electron concentration; $n_e \ll 10^{15}$ cm^{-3}) and highly conductive Nb-doped $SrTiO_3$ ($SrTi_{0.8}Nb_{0.2}O_3$, $n_e = 2.4 \times 10^{21}$ cm^{-3}) on the (001) face of $LaAlO_3$ single-crystal substrates by PLD at 900 °C in an oxygen atmosphere (oxygen pressure $P_{O_2} = 3 \times 10^{-3}$ Pa). During film growth of the superlattices, we monitored the intensity oscillation of the RHEED pattern in order to precisely control the layer thickness.

Figure 10 shows the Cs-corrected high-angle angular dark-field scanning transmission electron microscope (HAADF-STEM) image of a resultant superlattice, which clearly shows a stripe-shaped contrast. Furthermore, the intensity of the Ti column in one unit cell thickness of $SrTi_{0.8}Nb_{0.2}O_3$ showed a higher intensity than that of the $SrTiO_3$ barrier layer, confirming that the doped Nb^{5+} ions are exclusively confined in the $SrTi_{0.8}Nb_{0.2}O_3$ layer.

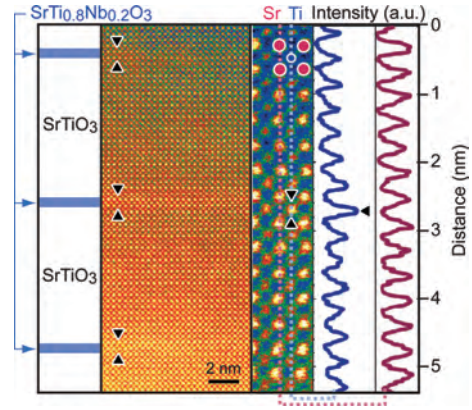

Figure 10. HAADF-STEM image of a $[(SrTiO_3)_{24}/(SrTi_{0.8}Nb_{0.2}O_3)_1]_{20}$ superlattice and intensity profiles across the Ti and Sr atomic columns. Stripe-shaped contrast is clearly seen. Furthermore, the intensity of the Ti column in one unit cell thickness of $SrTi_{0.8}Nb_{0.2}O_3$ shows a higher intensity than that of the $SrTiO_3$ barrier layer, confirming that the doped Nb^{5+} ions are exclusively confined in the $SrTi_{0.8}Nb_{0.2}O_3$ layer.

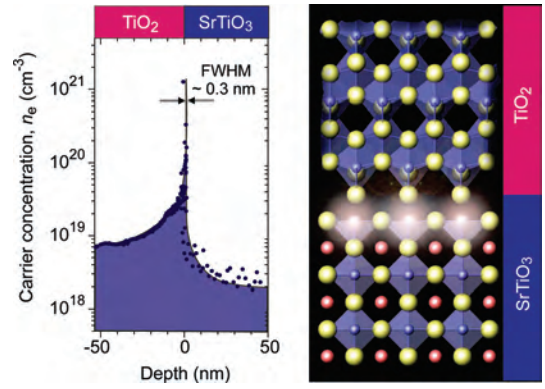

Figure 11. (left) Depth profile around the interface between a 56-nm-thick TiO_2 epitaxial layer and the $SrTiO_3$ substrate. An intense carrier concentration peak ($n_e \sim 1.4 \times 10^{21}$ cm^{-3}) with a FWHM of ~0.3 nm is observed at the $TiO_2/SrTiO_3$ interface. (right) Schematic drawing of the heterointerface.

A 2DEG was also formed at the heterointerface in $TiO_2/SrTiO_3$ because electrons in the conduction band should be localized at the heterointerface between TiO_2 and $SrTiO_3$ because of possible bending of the $SrTiO_3$ conduction band. Epitaxial films of TiO_2 were deposited on the (001) face of $SrTiO_3$ single-crystal plates by PLD using a ceramic TiO_2 (rutile) target at 700 °C in an oxygen atmosphere (oxygen pressure $P_{O_2} = 3 \times 10^{-3}$ Pa). Oxygen-deficient $TiO_{2-\delta}$ is likely formed by the PLD process under a low-oxygen atmosphere. The deposited film may extract oxide ions (O^{2-}) from the $SrTiO_3$ substrate, which results in the formation of carrier electrons confined at the interface of $TiO_2/SrTiO_3$.

Figure 11 shows the depth profile for the $TiO_2/SrTiO_3$ heterointerface. A steep peak with n_e of ~1.4×10^{21} cm^{-3} was observed at the heterointerface of $TiO_2/SrTiO_3$. The full width at half-maximum (FWHM) of the peak was ~0.3 nm, which agrees well with the lattice parameter of $SrTiO_3$ (a = 0.3905 nm) and indicates that the high-density carrier

(59) Meyers, M. A., Inal, O. T., Eds. *Frontiers in Materials Technologies*; Elsevier: Amsterdam, The Netherlands, 1985.
(60) Hicks, L. D.; Dresselhaus, M. S. *Phys. Rev. B* **1993**, *47*, 12727.
(61) Hicks, L. D.; Harman, T. C.; Sun, X.; Dresselhaus, M. S. *Phys. Rev. B* **1996**, *53*, 10493.

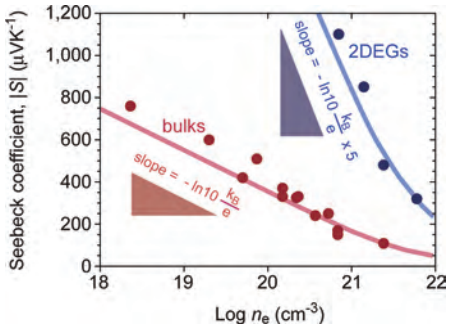

Figure 12. $|S|_{300\ K}$−log n_e plots for the 2DEGs and the $SrTiO_3$ bulk samples. The slope of $|S|_{300\ K}$ for 2DEGs is ∼−1000 $\mu V \cdot K^{-1}$, which is ∼5 times greater than that for the $SrTiO_3$ bulk (−198 $\mu V \cdot K^{-1}$).[20]

electrons ($n_e \sim 7.0 \times 10^{20}$ cm^{-3}) are localized within the thickness of a unit cell layer of $SrTiO_3$ at the heterointerface. Additionally, this observation clearly demonstrates that a 2DEG is formed at the heterointerface in $TiO_2/SrTiO_3$.

Figure 12 shows the $|S|$−log n_e plots, which verify that the experimental data points for the 2DEGs and the $SrTiO_3$ bulk samples form two straight lines with different slopes. The relationship between $|S|$ and n_e is simply explained by the following equation:[62] $|S| = -k_B/e \ln 10\ A(\log n_e + B)$, where k_B is the Boltzmann constant. A and B are parameters that depend on the types of materials and their energy band structures: For instance, A was equal to 1 for a 3D energy band with a parabolic DOS near the Fermi surface, which makes it difficult to enhance the $S^2\sigma$ value for $SrTiO_3$ bulks because the slope of the $|S|$−log n_e line gives a constant value of $-k_B/e \ln 10$ (−198 $\mu V \cdot K^{-1}$). On the other hand, the slope of the $|S|$−log n_e line for the 2DEGs was −1000 $\mu V \cdot K^{-1}$. Because the slope provides the A value, this clearly demonstrates that the $|S|$ value for the 2DEGs is enhanced by a factor of ∼5 relative to that of the $SrTiO_3$ bulk.

(62) Jonker, G. H. *Philips Res. Rep.* **1968**, *23*, 131.

5. Summary

We measured the intrinsic thermoelectric properties of p-type $Ca_3Co_4O_9$ and n-type $SrTiO_3$:Nb using high-quality epitaxial films and compared our results to the literature values. Although very high ZT values ∼ 1 have been reported, reliable ZT values of both materials were clarified to be ∼0.05 at 300 K and ∼0.3 at 1000 K. Thus, nanostructural control such as an artificial superlattice or 2DEG may be necessary to obtain a high ZT thermoelectric oxide. For example, the present approach utilizing a 2DEG in $SrTiO_3$ may provide a new route to realizing practical thermoelectric materials without employing toxic heavy elements.

Acknowledgment. The authors gratefully acknowledge Profs. S.-W. Kim (Tokyo Tech), M. Hirano (Tokyo Tech), H. Hosono (Tokyo Tech), and Y. Ikuhara (University of Tokyo) for their helpful discussions. The authors also thank Dr. K. Nomura (ERATO-SORST, JST) for his precise analysis of the 2DEG samples, Prof. T. Mizoguchi (University of Tokyo) for HAADF-STEM observations of superlattice samples, and T. Saito (JFCC) for HRTEM observations of the layered cobalt oxide films. This work was financially supported by the Industrial Technology Research Grant Program in 2005 from the New Energy and Industrial Technology Development Organization (NEDO) and a Grant-in-Aid for Scientific Research from the Ministry of Education, Culture, Sports, Science and Technology (Grant 18686054).

IC800644X